Journal of Materials Chemistry B

ROYAL SOCIETY OF CHEMISTRY

PAPER

View Article Online
View Journal | View Issue

Check for updates

Cite this: J. Mater. Chem. B, 2023, 11, 10929

Exploring the antimicrobial potential of isoniazid loaded Cu-based metal–organic frameworks as a novel strategy for effective killing of *Mycobacterium tuberculosis*†

Pawan Kumar,‡[a] Ananyaashree Behera,‡[b] Pranav Tiwari,[a] Sibi Karthik,[c] Mainak Biswas,[b] Avinash Sonawane[bc] and Shaikh M. Mobin *[acde]

Tuberculosis (TB) remains one of the most infectious pathogens with the highest human mortality and morbidity. Biofilm formation during *Mycobacterium tuberculosis* (*Mtb*) infection is responsible for bacterial growth, communication, and, most essentially, increased resistance/tolerance to antibiotics leading to higher bacterial persistence. Thus, biofilm growth is presently considered a key virulence factor in the case of chronic disease. Metal–Organic Frameworks (MOFs) have recently emerged as a highly efficient system to improve existing antibiotics' therapeutic efficacy and reduce adverse effects. In this regard, we have synthesized Cu-MOF (**IITI-3**) using a solvothermal approach. **IITI-3** was well characterized by various spectroscopic techniques. Herein, **IITI-3** was first encapsulated with isoniazid (**INH**) to form **INH@IITI-3** with 10 wt% loading within 1 hour. **INH@IITI-3** was well characterized by PXRD, TGA, FTIR, and BET surface area analysis. Furthermore, the drug release kinetics studies of **INH@IITI-3** have been performed at pH 5.8 and 7.4 to mimic the small intestine and blood pH, respectively. The results show that drug release follows first-order kinetics. Furthermore, the antimycobacterial activity of **INH@IITI-3** demonstrated significant bacterial killing and altered the structural morphology of the bacteria. Moreover, **INH@IITI-3** was able to inhibit the mycobacterial biofilm formation upon treatment and showed less cytotoxicity toward the murine RAW264.7 macrophages. Thus, this work significantly opens up new possibilities for the applications of **INH@IITI-3** in biofilm infections in *Mtb* and further contributes to TB therapeutics.

Received 2nd October 2023,
Accepted 24th October 2023

DOI: 10.1039/d3tb02292g

rsc.li/materials-b

Published on 24 2023. Downloaded on 29/07/25 17:07:55.

1. Introduction

Mycobacterium tuberculosis (Mtb), the causative agent of human tuberculosis (TB), remains one of the deadliest pathogens, infecting approximately 10 million people globally with 1.3 million death cases annually.[1] Primarily, TB affects the lungs, known as pulmonary TB, and the treatment regime involves six months long administration of multiple antibiotics where patients in the initial two months intensive phase are given four first-line antibiotics, *i.e.*, isoniazid (INH), rifampicin (RIF), ethambutol (EMB), and pyrazinamide (PZA) followed by a four-month continuation period where patients are given **INH** and RIF.[1–3] Multidrug resistant (MDR) TB continues to be a public health emergency with severe health safety threat. The continuous and frequent administration of multiple drugs leads to low or non-adherence towards the therapy; moreover, toxic side effects such as gastrointestinal (GI) upset, fever, rash, *etc.* due to multiple dosing along with a longer duration of treatment also lead to defiance towards the therapy resulting in the emergence of drug-resistant strains among non-compliance patients.[4,5] Partial/incomplete clearance of tubercle bacilli often results in reversion of the disease thereby recurrence of persistent drug-tolerant bacteria. Thus, both drug resistance and drug persistence are primary concerns in the case of TB and are also associated with biofilm formation.[6]

[a] *Department of Chemistry, Indian Institute of Technology, Indore, Simrol, Madhya Pradesh, India*
[b] *School of Biotechnology, KIIT Deemed to be University, Bhubaneswar, Odisha, India. E-mail: xray@iiti.ac.in; Tel: +91-731-2438752*
[c] *Department of Biosciences and Biomedical Engineering, Indian Institute of Technology, Indore, Simrol, Madhya Pradesh, India*
[d] *Center for Advance Electronic (CAE), Indian Institute of Technology, Indore, Simrol, Madhya Pradesh, India*
[e] *Center for Electric Vehicle and Intelligent Transport Systems, Indian Institute of Technology, Indore, Simrol, Madhya Pradesh, India*

† Electronic supplementary information (ESI) available: The experimental section includes the synthesis of the H_4L linker, its characterization studies (mass spectrometry, NMR spectroscopy), activation of **IITI-3** (PXRD), linearity plot, DLS hydrodynamic average particle size, kinetic models, and zeta potential. See DOI: https://doi.org/10.1039/d3tb02292g

‡ Pawan Kumar (Design and synthesis of Cu-MOF, characterization and drug delivery) and Ananyaashree Behera (Involved in Biological studies) contributed equally to this work.

Published on 24 2023. Downloaded on 29/07/25 17:07:55.

Many pathogens, including *Mtb*, *Staphylococcus aureus*, and *Pseudomonas aeruginosa*, are known to form biofilms.[6,7] Biofilms are functionally heterogeneous clusters of microcolonies or single cells of replicating and non-replicating bacteria, swathed in a milieu of autogenous extracellular polymeric molecules attached to organic or abiotic surfaces or to each other.[7,8] Mycobacterial biofilms and persistent cells are mostly formed because of stress and quorum sensing. Biofilm development starts with bacterial adherence, followed by various stages of surface attachment, sessile growth, matrix synthesis, and dispersal.[9] Biofilm formation is an ingrained mechanism of antibiotic resistance, among others, where it provides protection against antibiotics to several bacterial species that are typically effective against identical bacteria in a planktonic state.[9,10] Studies suggest that the minimum bactericidal concentration (MBC) of antibiotics for biofilm eradication is usually higher than the planktonic bacterial cells, thus making it difficult for biofilm treatment by conventional antibiotic administrations due to the toxicity and side effects of higher doses of antibiotics.[10] Various mechanisms have been involved in this antibiotic resistance, such as permeability, persisted cells, activation of resistance genes, and metabolic states.[11] Moreover, biofilm formations are associated with various infections, which may result in treatment failures and other medical complications, as antibiotic therapy is solely incompetent in eradicating sessile organisms.[12,13] To overcome these complications, there is a requirement for the development of new drug targets as well as potential therapeutic applications, which harbor higher efficacy to penetrate and destruct the biofilms and enter intracellular targets, thereby eliminating the bacteria.

A regulated and sustained drug delivery system can support reducing adverse effects and improving the therapeutic efficacy.[14] Control over guest release profiles can be found by selecting different types of functional groups of the linker and fine-tuning the pore size.[15] Furthermore, it can inhibit the establishment of drug-resistant species since changes in the drug content will leave bacteria with little time to adapt. Several advanced biomaterials, including biopolymer, silica, and lipid-based materials, have been created to improve the effectiveness of drug delivery systems.[16–19] Despite the increasing advancement of biomaterials for drug delivery systems, inadequate drug loading, and controlled drug delivery due to the material's tiny pore volume remains an unacceptable aspect.[20]

A large pore volume material was developed recently known as Metal–Organic Frameworks (MOFs) to address these issues.[21–25] MOFs are porous materials with topologies composed of inorganic single ion or ion cluster nodes connected by organic linkers *via* covalent, non-covalent, and different types of non-covalent interactions.[26–34] They have a large surface area, tunable pore size, and are biocompatible as well as hemocompatible.[35–39] MOFs have been used in a wide range of applications such as catalyst, gas adsorption/separation, sorbet for the preparation of different analytical samples, solid phase extraction of hydrocarbons, dye degradation, solar cells, *etc.*[40–47] MOFs' bioapplication mainly include drug delivery, biosensing, bioimaging, phototherapy, wound healing, antibiotic detection in food, *etc.*[48–54] Drugs are loaded within the pores and surface of the MOFs *via* some covalent, non-covalent interactions (in the case of neutral drugs) and some electrostatic hydrophilic/hydrophobic interactions (in the case of ionic drugs).[55,56] In 2019, Simon *et al.*[57] performed isoniazid drug delivery using MIL-100(Fe) MOFs for the first time. Similarly, Gaweł *et al.*[58] and Acharya *et al.*[59] performed the isoniazid drug delivery using Fe-MIL-101-NH_2 and BIO-MOF-100 but did not determine the antibacterial activity of the released isoniazid. A study by Sun *et al.*, 2017 demonstrates the application of mixed ligand Cu-MOFs (MOFs-2) as a drug delivery vehicle for the release of an anthracycline antibiotic, Doxorubicin hydrochloride (DOX). MOFs-2 exhibited the highest efficiency in DOX loading without affecting the structure of MOFs-2 and complete DOX release from DOX@MOFs-2 was observed in acidic solution (pH 3.8).[60] DOX is also known to be a potent inhibitor of *Mtb* DnaG and demonstrates effective antibacterial activity against *Msm* and *Mtb*.[61] Thus, DOX encapsulated MOFs could be potentially useful as a therapeutic agent for sustained drug delivery and antibacterial activity against drug resistant TB.

In the present study, we have synthesized a Cu(II) based MOF named **IITI-3** using our previously reported method,[62] which has a large surface area (1258 $m^2\ g^{-1}$) and is mesoporous in nature (having a pore diameter of 3.420 nm).[63] Encouraged by our recent work, which showcases controlled insulin delivery by **IITI-3**, prompted us to explore this towards TB therapeutics. The *in vitro* cytotoxicity investigations of **IITI-3** validated its safety, and the accumulation detected in the cell cytoplasm suggests potential utility in the treatment of pulmonary tuberculosis. After that, we incorporated **IITI-3** with the **INH** drug and performed drug release kinetic studies under different conditions. Next, we demonstrated that upon treatment of *M. smegmatis* (*Msm)* and *M. bovis* BCG (BCG), the non-pathogenic laboratory strains of *Mtb* with **INH@IITI-3**, there was significant reduction in the bacteria count and altered the bacterial morphology. **INH@IITI-3** treatment inhibited biofilm formation in *Msm* and the pellicle formed between air–liquid interfaces were loose and detached. However, no difference was observed in the biofilm disruption assay. Additionally, comparative cytotoxicity analysis was checked and **INH@IITI-3** exhibited a less cytotoxic effect on the host RAW 264.7 macrophages. Together, these observations indicate that **INH@IITI-3** could have significant implications in eradicating mycobacterial biofilms by preventing biofilm development and it could be an intriguing substitute for the standard TB therapy. Nevertheless, further studies of **INH@IITI-3** against the pathogenic strains of *Mtb* are essential for better understanding the activity and functionality of drug-based MOFs.

2. Materials and methods

2.1 Materials

All reagents were commercially procured and were used without any further purification. $Cu(NO_3)_2{\cdot}3H_2O$ (98%), 5-hydroxyisophthalic acid, 2,6-bis(bromomethyl)pyridine, DMF, HCl, EtOAc, Na_2SO_4, K_2CO_3, H_2SO_4, and isoniazid were purchased from

 This journal is © The Royal Society of Chemistry 2023

Published on 24 2023. Downloaded on 29/07/25 17:07:55.

Sigma-Aldrich, Loba Chemie and S. D. Fine Chemicals (India), respectively.

2.2 Synthesis of H_4L

H_4L was synthesized by the previously reported method.[62] In the first step, a simple substitution reaction takes place between 5-hydroxyisophthale and 2, 6-bis(bromomethyl)-pyridine to form diethyl 5-((6-((3-(ethoxycarbonyl)-5-(propionyloxy)phenoxy)methyl)pyridin-2-yl)methoxy)isophthalate in the presence of potassium carbonate and acetonitrile solvent under a N_2 atmosphere. In the second step, the basic hydrolysis takes place, resulting in the formation of 5,5′-((pyridine-2,6-diylbis(methylene))bis(oxy))diisophthalic acid (**H_4L**). The detailed synthetic procedure with characterization (Fig. S1–S6) is given in the ESI.†

2.3 Synthesis of IITI-3

The preparation method of **IITI-3** has been taken from our previously reported method.[62] In this method, **H_4L** (0.040 g, 0.043 mmol), $Cu(NO_3)_2{\cdot}3H_2O$ (0.112 g, 0.23 mmol), and 0.2 mL of 1 M HCL solution were combined with DMF (4.0 mL) and water (2.0 mL). This mixture was then agitated for 48 hours under high pressure in a Teflon-lined autoclave, and after completion of the reaction, it was cooled to room temperature at a rate of 1 °C min^{-1}. The **IITI-3** blue crystals were made. These crystals were dried in a vacuum oven after being constantly cleaned with water and acetone. (Yield = 79.8%) (Scheme 1).

2.4 Activation of IITI-3

IITI-3 was synthesized in a DMF/water solvent system, so there is a high probability that these solvent molecules may be present within the framework and occupy some space within the pores. So, to create a solvent-free and highly porous framework, before utilizing it as the drug delivery carrier, we have activated **IITI-3**. The synthetic material was activated using a solvent exchange experiment.[64,65] In this experiment, we have taken acetone as a solvent because acetone does not disturb the structural integrity of the framework. This experiment took place over seven consecutive days and twice a day.

Further heating of the solvent-exchanged sample at 130 °C for 6 hours under extreme vacuum resulted in the formation of additional pores and a solvent-free framework confirmed by the color changes of **IITI-3** from blue to dark blue, resulting in the loss of metal-bound water molecules (Fig. S7, ESI†). Activated **IITI-3** maintained the framework through the activation, which is confirmed by PXRD. PXRD data of activated **IITI-3** have all the significant peaks present in as synthesized **IITI-3** (Fig. S8, ESI†).

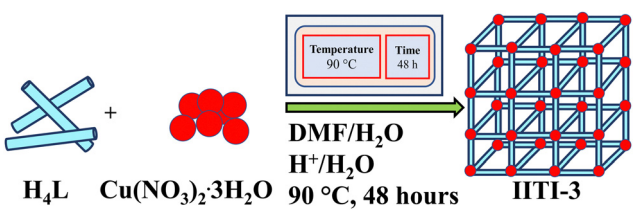

Scheme 1 Schematic synthesis of **IITI-3**.

2.5 INH encapsulation within THE IITI-3 framework

To encapsulate the isoniazid, the crystals of activated **IITI-3** were treated with the **INH** solution (DI water, 100 μg mL^{-1} at pH = 7.0) for continuous stirring at 200 rpm for 1 h at room temperature. The resulting solid composite was filtered, and the supernatant was collected. The excess INH molecules adhered to the surface of the **IITI-3** crystals and were removed by washing the solid composite with DI water three times.

2.6 *In vitro* INH release studies

A drug delivery experiment was performed using the dialysis technique. A definite amount (10 mg) of **INH@IITI-3** was placed in a culture tube and submerged in 10 mL of a solution with pH values of 5.8 and 7.4, continuously stirring at 200 rpm at room temperature. 2 mL of sample was taken at every finite time interval. The same volume of the new solution with the same pH was added to keep the volume constant. A UV-Vis spectrophotometer was used to quantify how much drug had been released (for **INH**, λ = 263 nm).

Using a linearity plot (Fig. S8, ESI†) and UV-Vis spectrometry, the loading and release characteristics of **INH** from **INH@IITI-3** were identified, and the drug loading content (DLC) was calculated according to the following formula,[66]

$$\text{Drug loading content (DLC)} = \frac{\text{weight of Isoniazid loaded in vehicle}}{\text{weight of Isoniazid loaded vehicle}} \times 100 \quad (1)$$

2.7 Bacterial strains and reagents

Mycobacterium smegmatis mc^2155 (*Msm*) and *Mycobacterium bovis* BCG (BCG) were grown in Middlebrook's 7H9 broth medium (271310, Difco, New Jersey, USA) containing 0.05% Tween80 at 37 °C at 120 rpm. *M. bovis* BCG was supplemented with 10% OADC (oleic acid-albumin-dextrose-catalase) (FD018, Himedia, India). Mouse macrophage RAW264.7 cells were maintained in DMEM (Dulbecco's modified Eagle's medium) (10566016, Gibco, Invitrogen, USA) supplemented with 10% fetal bovine serum (FBS) (10270106, Gibco, Invitrogen, USA) at 37 °C. Cell Counting Kit-8 (CCK-8) (CK04-13) was procured from Dojindo Molecular Technologies (Japan). Sauton's Fluid medium base (M1276, Himedia, India) was used to grow a mycobacterial biofilm. Crystal violet (28376) staining was obtained from Sisco Research Laboratories (SRL), India. Acridine orange (MB116) was procured from Himedia, India.

2.7.1 *In vitro* killing assay. The antimycobacterial activity of **IITI-3**, **INH@IITI-3**, and **INH** was determined in *Msm* and BCG as described in Pati *et al.*, 2016.[67] Briefly, 4–5 × 10^5 bacteria were incubated with several concentrations of these molecules in 7H9 medium for 24 hours. Bacteria were harvested, and the colony forming unit (CFU) enumeration was performed by plating serially diluted cultures on 7H9 agar

Published on 24 2023. Downloaded on 29/07/25 17:07:55.

plates. All samples were plated in triplicates, and CFU plotting was performed using GraphPad Prism software. The values were an average of three independent experiments.

2.7.2 Field emission – scanning electron microscopy (FE-SEM) analysis. *Msm* was grown to the mid-logarithmic phase and treated with **IITI-3** and **INH@IITI-3** at a final concentration of 25 μg mL^{-1} and **INH** at a final concentration of 2.5 μg mL^{-1}. 24 hours post-treatment, treated *Msm* samples were drop cast on glass slides and kept for air drying. The samples were fixed with 2.5% glutaraldehyde at rt for 1 h. Samples were dehydrated using increasing gradients of ethanol up to 100% and kept in a desiccator overnight. The samples were coated using gold sputter coating for 120 s, followed by observation by FE-SEM (Carl Zeiss).

2.7.3 Crystal violet staining. Mid-log phase *Msm* was pelleted and washed with 1× PBS, resuspended in Sauton's medium, and the OD_{600} was adjusted to 0.5. Bacteria were incubated with and without **IITI-3**, **INH@IITI-3**, and **INH** in 12 well plates and incubated at 37 °C at static conditions. Post 5 days of incubation, media was removed from the treated and untreated bacteria, and crystal violet (0.1% w/v in H_2O) was added in each well and incubated for 30 min. The wells were washed with 1× PBS, and the bound dye was extracted using methanol : ethanol (7 : 3) solution for 1 hour, followed by spectrophotometric quantification at 595 nm.

2.7.4 Acridine orange staining by confocal laser scanning microscopy. *Msm* was grown until the mid-log phase, pelleted, and washed with 1× PBS. The bacteria were resuspended in Sauton's medium and grown on sterile coverslips treated with different drugs, as discussed above. Untreated bacteria were used as the control. The media was discarded and washed with 1× PBS. Biofilms were fixed with 4% formaldehyde for 20 min in the dark at room temperature. The fixing solution was discarded and washed with 1× PBS. Biofilms are stained with 0.2% Acridine orange dye and incubated in the dark for 15 min. The coverslips were mounted using 10% glycerol, sealed, and visualized using Confocal Laser Scanning Microscopy (CLSM) (Olympus IX83, Tokyo, Japan). The images were acquired and processed using Fluoview.

2.7.5 Pellicle formation assay. To check the pellicle formation, *Msm* was grown in borosilicate glass tubes containing Sauton's medium. A bacterial culture was prepared as described above, and an equal number of bacteria with different drugs was inoculated into tubes containing 4 mL of Sauton's medium and incubated at 37 °C at static conditions. Untreated *Msm* was used as control. After seven days of incubation, the pellicle formation was observed and photographed.[68] Bacterial enumeration was performed by mechanically disturbing the pellicles using a syringe, followed by serial dilution of the cultures, plating on 7H9 agar plates, and incubating the plates at 37 °C for 36 hours.

2.7.6 Cytotoxicity assay. RAW 264.7 macrophages (1×10^4 cells per well) were grown in a 96 well plate for 24 hours, followed by treatment with different concentrations of **IITI-3**, **INH@IITI-3**, and **INH** (loading content) for another 24 hours. Cell viability was performed using the CCK-8 kit per the manufacturer's protocol.

2.7.7 Statistical analysis. GraphPad Prism (Prism 5.0, San Diego, CA, USA) was used to generate the graphs. Statistically significant differences between groups were determined by one-way Analysis of Variance (ANOVA) using Dunnett's Multiple Comparison Test. Experiments were performed in triplicates. Significance was referred to as * for $p \leq 0.05$, ** for $p \leq 0.01$, and *** for $p \leq 0.001$ and ns for non-significant.

3. Results and discussions

3.1 Preparation and characterization of IITI-3, INH@IITI-3

The preparation process of **IITI-3**, **INH@IITI-3**, is depicted in Schemes 1 and 2, respectively.

First, the **IITI-3** has synthesized using solvothermal approach by combining $\mathbf{H_4L}$ and $Cu(NO_3)_2{\cdot}3H_2O$ in DMF and water (2 : 1) under acidic conditions and then heating to 90 °C for 48 hours. Blue-colored crystals were produced. The produced crystals of **IITI-3**'s structure were evaluated using a variety of characterization techniques.

A powder X-ray diffractometer (PXRD) has been recorded and compared with the previously reported **IITI-3** MOF to check the phase purity of as-synthesized material.[62] Most of the peaks were matched with the as-synthesized material. Some different, less intense peaks are present due to the solvent molecules in the lattice. After solvent exchange, activation, and **INH** encapsulation, the framework maintained its crystallinity, as confirmed by PXRD in Fig. 1(a). To evaluate the functional group within **IITI-3**, Fourier Transfer Infrared (FT-IR) spectra have been recorded. In the FT-IR spectra of **IITI-3**, one low intense peak at 3451 cm^{-1} corresponds to the water molecule present in the framework, and two peaks at 1631 and 1377 cm^{-1} correspond to asymmetric and symmetric vibrations of the carboxylate ion.[69] Two peaks around 1577 and 774 cm^{-1} confirm the presence of a pyridyl ring within **IITI-3**.[70–72] After **INH** encapsulation, all the significant peaks present in **INH@IITI-3** exactly match with the **IITI-3**, confirming that after encapsulation **IITI-3** maintained their

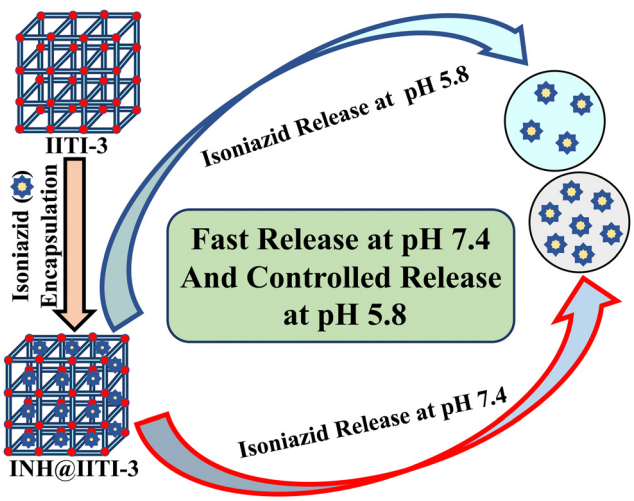

Scheme 2 Systematic scheme of INH encapsulation and release from **INH@IITI-3**.

This journal is © The Royal Society of Chemistry 2023

Published on 24 2023. Downloaded on 29/07/25 17:07:55.

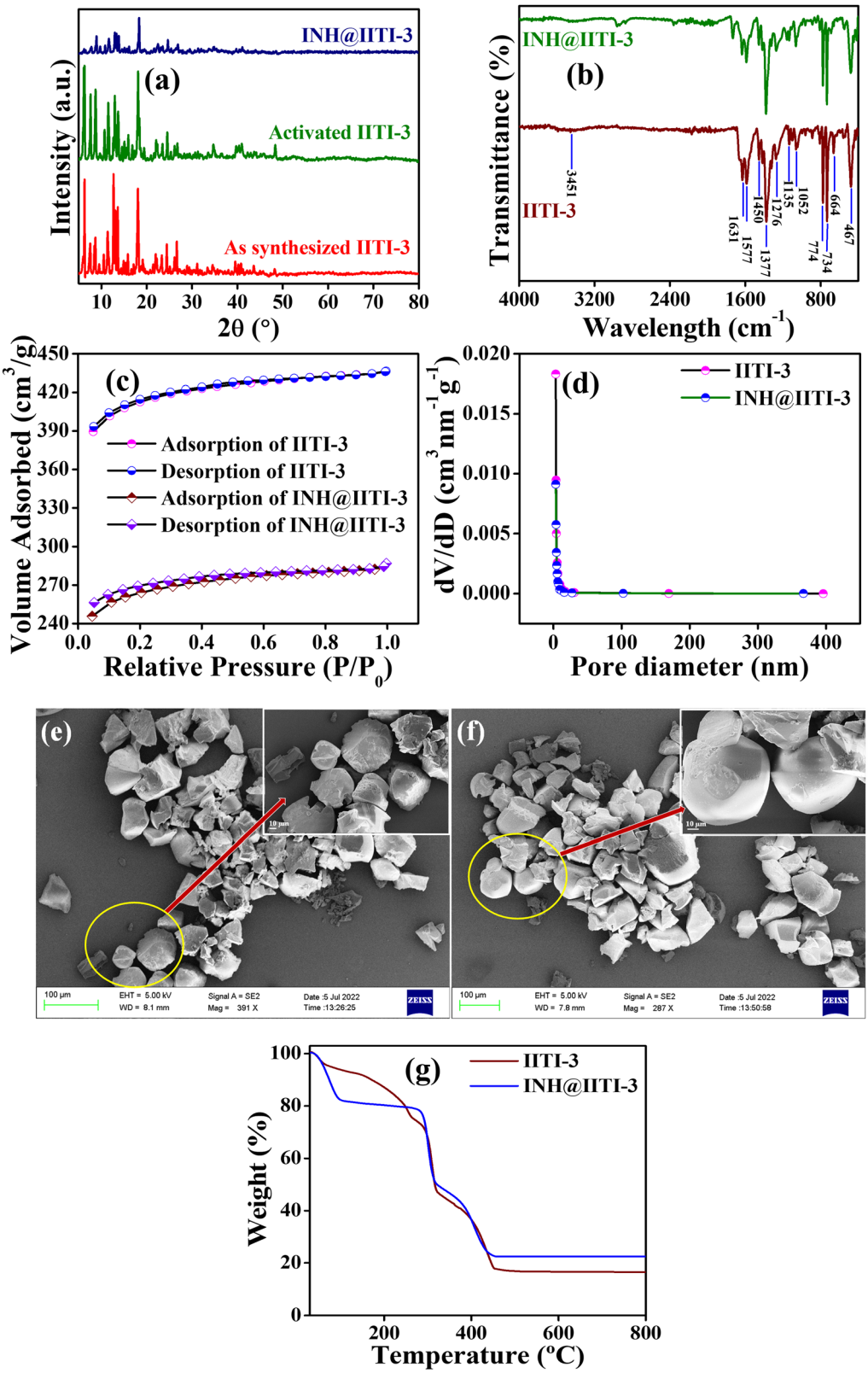

Fig. 1 (a) PXRD of as synthesized **IITI-3**, activated **IITI-3** and **INH@IITI-3**, (b) FT-IR data of **IITI-3** and **INH@IITI-3**, (c) BET surface area analysis of **IITI-3** and **INH@IITI-3**, (d) BJH pore size distribution of **IITI-3** and **INH@IITI-3**, (e) and (f) SEM analysis of **IITI-3** and **INH@IITI-3** at 100 and 10 μm magnification respectively, and (g) TGA of **IITI-3** and **INH@IITI-3**.

Published on 24 2023. Downloaded on 29/07/25 17:07:55.

functionality (Fig. 1b). MOFs are well known for their enormous surface area, and BET analysis has been performed for this. Results show that **IITI-3** has a high surface area of 1258 $m^2 g^{-1}$ and is mesoporous with a pore diameter of 3.420 nm.[63,73,74] After encapsulation, **INH@IITI-3** has less surface area of 803.21 $m^2 g^{-1}$ and a decrease in pore diameter of 3.346 nm compared to **IITI-3**, confirming that **INH** is present within the pore as well as on the surface of **IITI-3** (Fig. 1c and d).

Field emission surface electron microscopy (FE-SEM) has been performed to know the surface morphology of **IITI-3**. The results show that the **IITI-3** has an irregular cuboid-type of shape. After **INH** encapsulation, **INH@IITI-3** has a similar surface morphology as **IITI-3**, revealing no morphology changes after **INH** encapsulation (Fig. 1e and f). The thermal stability of the framework **IITI-3** is confirm by Thermogravimetric analysis (TGA). The TGA graph shows a 25% decrease in weight percent from 70 to 260 °C, corresponding to the removal of guest molecules (water/DMF) from the lattice. From 296 to 320 °C the framework starts breaking, and from 320 to 458 °C framework ultimately reaches elemental form. And beyond 458 °C, after increasing the temperature, no peak is observed, confirming that the framework completely goes into elemental state. After **INH** encapsulation, there is an increase in weight percent in the TGA graph of **INH@IITI-3**, confirming that **INH** is successfully encapsulated within the framework of **IITI-3** (Fig. 1g). From Dynamic light scattering (DLS), the average hydrodynamic size of **INH@IITI-3** is calculated at 689.4 nm, which is increased from 392.1 nm due to **INH** encapsulation (Fig. S10, ESI†).

3.2 Drug loading content and *in vitro* drug release kinetics

A 10 wt % **INH** loading is achieved within 1 h of encapsulation, calculated from eqn (1). The drug is encapsulated within the pore and on the surface of the framework, confirm by the BET analysis. After **INH** loading within **IITI-3**, **INH** goes to inside the pore and some amount is also present on the surface of the **IITI-3**. **IITI-3** upheld the **INH** *via* various interactions like Electrostatic (hydrophilic and hydrophobic), hydrogen bonding, van der Waals, coordination bonds and some π–π interaction.[75–77] As **INH** is a neutral small molecule it possibly goes inside the pore and will be held *via* covalent, π–π interaction and some hydrogen bond interaction. After successfully calculating the loading percentage, *in vitro* drug release studies from **INH@IITI-3** have been performed at pH 5.8 and 7.4 to mimic the small intestine and blood pH, respectively.[78] The drug release from **INH@IITI-3** was due to the diffusion process.[58] In this process the **INH** comes out from the higher concentration region to the lower concentration region.[79,80] When we performed the drug delivery experiment, we suspended the 10 mg of **INH@IITI-3** in the 10 mL of solution. **INH** started to come out from **INH@IITI-3** to the solution due to the concentration difference. As in the dialysis method, the same amount (in our case, 2 mL) of the solution is taken out after a fixed time and maintained the same volume by fresh solution resulting the more concentration difference and more drug release.

The drug release experiments have performed by gentle stirring at 200 rpm. The drug release model is described mainly from three types of models Higuchi (eqn (2)),[81] Zero order (eqn (3)),[81] and First order (eqn (4)),[82] which are as follows:

$$R = k_H \sqrt{t} \quad (2)$$

$$R = q_0 + k_0 t \quad (3)$$

$$R = R_e(1 - e^{-kt}) \quad (4)$$

where; R = cumulative drug release, k_H, k_0, k is the constant of Higuchi, zero, and first-order kinetics, respectively. The parameters q_0, R_e, and t denote the starting amount of **INH**, the percentage of **INH** release at equilibrium time (h), and release time (h), respectively. Subsequently, a successful fit to the Higuchi model indicates drug release from a planar heterogeneous matrix system *via* the pore matrix.[83,84] A good fit to the zero-order model reveals that the release system is an osmotic and transdermal system.[84,85] The release system of water-soluble drugs in a non-swelling porous matrix is described as a good fit for the first-order model.[86]

The model fitting into the drug release profile from **INH@IITI-3** is shown in Fig. 2, Fig. S11 (ESI†). And parameter for the fitting of different models is given in Table 1. We have fitted in the Higuchi kinetic model, zero order, and first-order model, but the fitting parameter and analysis clearly show that the drug release follows 1st order kinetics which corresponds to the drug release from the porous matrices.[14,84] This suggests that the drug is released continuously and at different rates.[87] The experimental cumulative drug release (R) value after 24 hours is 39.08% and 43.47% at pH 5.8 and 7.4, respectively. From the first-order kinetic model, it is calculated from 35.91% and 39.33%, which is well matched with the calculated one.

The drug release was comparably high in alkaline pH, because at higher pH, after releasing the **INH**, positively charged sites are vacant and the negatively charged OH^- from the alkaline solution stabilizes the **IITI-3** framework.[57] This is

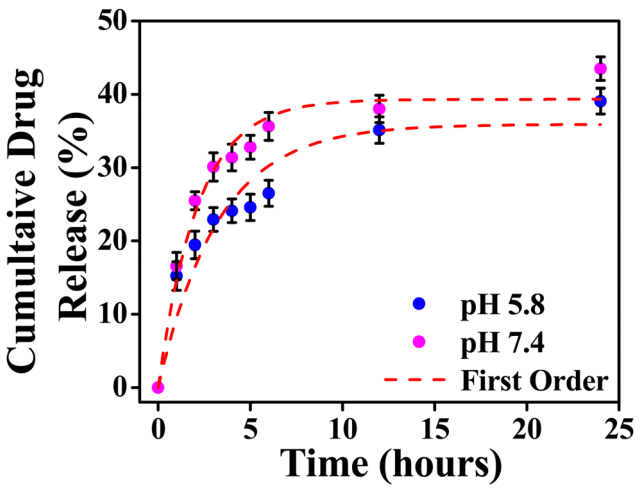

Fig. 2 Cumulative drug release from **INH@IITI-3** at pH 5.8 and 7.4 with first order kinetics respectively.

This journal is © The Royal Society of Chemistry 2023

Published on 24 2023. Downloaded on 29/07/25 17:07:55.

Table 1 Release kinetics parameter (Higuchi, zero and first order) from INH@IITI-3 at 5.8 and 7.4 pH, respectively

Model	Parameter	pH 5.8	pH 7.4
Higuchi	k_H	9.88922 ± 0.67901	11.80515 ± 1.10224
	R^2	0.79465	0.59184
Zero order	k_0	1.12194 ± 0.33423	1.2345 ± 0.46172
	R_e, %	15.26069 ± 3.17272	20.3483 ± 4.38294
	R^2	0.6072	0.43458
First order	k	0.30763 ± 0.0584	0.46443 ± 0.05691
	R_e, %	35.9153 ± 2.56969	39.33457 ± 1.46521
	R^2	**0.90805**	**0.96826**

confirmed by the zeta potential value of **INH@IITI-3**, −23.5, and −25.6 at pH 5.8 and 7.4, respectively (Fig. S12, ESI†). There is a slight increase in zeta potential leading to a slight increase in drug delivery. The increased negative value of zeta potential will cause more positively charged sites present on the surface.[88] And at pH 7.4, a greater number of positively charged sites are stabilized in comparison to lower pH 5.8. This concludes that at 7.4 pH, **INH** release is comparatively higher with respect to pH 5.8, leading to higher zeta potential.[89] This will cause interference in interactions between **INH** molecules and the active surface of **IITI-3**.

3.3 Evaluation of antimycobacterial efficiency of the compounds

The synthesized **IITI-3**, **INH@IITI-3**, and free **INH** were tested against *Msm* and BCG to assess their antimycobacterial activity. The results obtained against the assayed *Msm* indicate a significant decrease in the antibacterial activity of **IITI-3**, **INH@IITI-3**, and free **INH** when compared with the buffer control after 24 hours of treatment (Fig. 3A). Significant killing of *Msm* when treated with **IITI-3** alone indicates that MOFs, especially Cu-MOFs, can also release metal ions, which can destruct the cellular integrity, thereby killing the bacteria.[90] Several studies have shown the synergistic effect of antibiotics when incorporated in MOFs. The release of metal ions from the MOFs concurrent with the antibiotic effect on the bacteria synergistically augments the antibacterial activity,[91,92] which herein, with the treatment of **INH@IIT-3**, substantial *Msm* killing was observed (Fig. 3A). The cell wall of mycobacteria is crucial for its viability and virulence. There are two probable mechanisms for MOFs to incapacitate/eradicate bacteria. Leaching of metal ions from the MOFs or the interactions between the active sites of MOF surfaces and the bacterial surface to peroxidise bacterial membrane lipids, thus disrupting the membrane.[93] However, interestingly, we did not observe a significant reduction in the bacterial count when BCG was

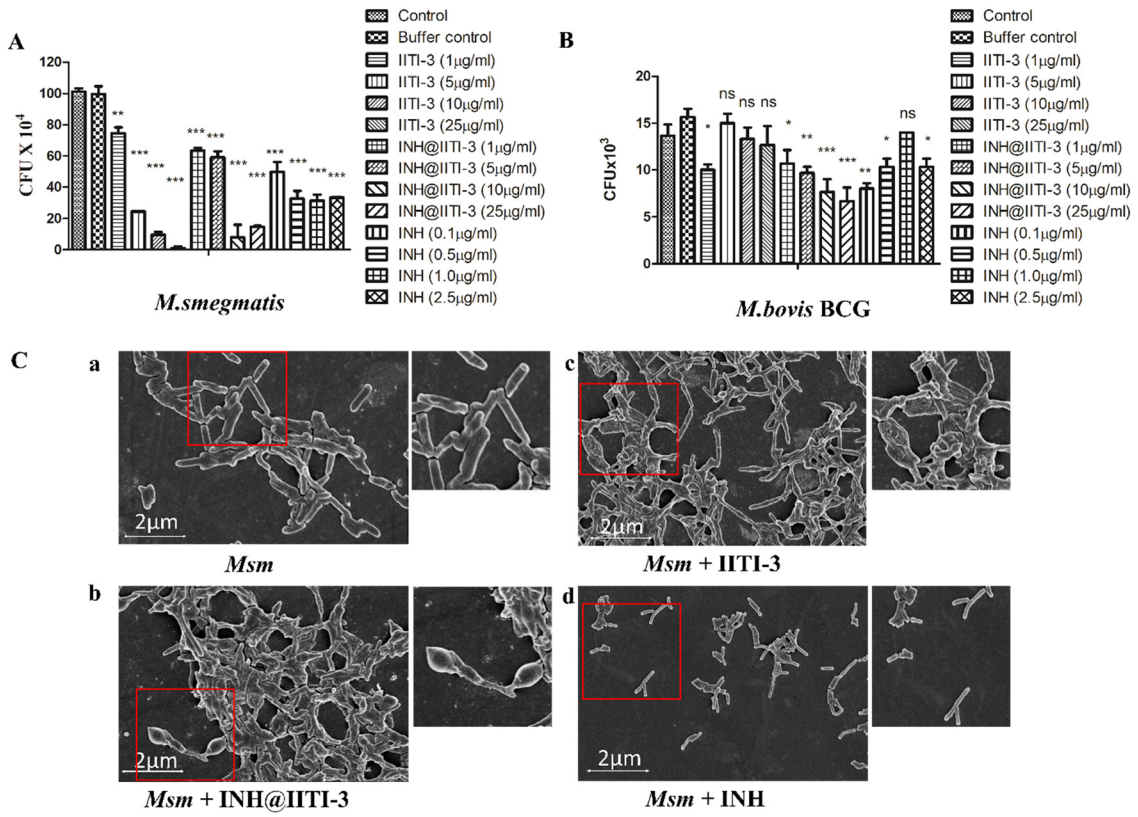

Fig. 3 Antibacterial activity of **INH@IITI3** was determined against (A) *M. smegmatis* and (B) *M. bovis* BCG. Bacteria were incubated with different concentrations of **IITI-3**, **INH@IITI-3** and **INH** for the indicated time point and bacterial survival was determined by the CFU assay. (C) FE-SEM of *M. smegmatis*: (a) Control, (b) with **INH@IITI-3** treatment, (c) with **IITI-3** treatment, and (d) with **INH** treatment. *Msm* was analysed for morphological variations with different treatments of the compounds.

Published on 24 2023. Downloaded on 29/07/25 17:07:55.

treated with only **IITI-3** (Fig. 3B). This might be because of the several virulence factors of BCG and its distinctive cell envelope that is not affected only by the Cu(II) ions. However, further studies are a prerequisite to establishing the MOF mechanism of action against BCG. Next, we observed significant killing of BCG with increasing concentration of **INH@IITI-3** when compared with **IITI-3** and free **INH** (Fig. 3B). The probable reason for significant bacterial reduction might be the synergistic effect of **INH** together with the Cu(II) ions. However, there is a necessity for detailed evaluation regarding the MOF activity against BCG for a better understanding of the mechanism.

Furthermore, we visualized the effects of **IITI-3** and **INH@IITI-3** on the morphology of *Msm* using a field emission scanning electron microscope (FE-SEM). The exposure of *Msm* to 25 μg mL^{-1} **IITI-3** or **INH@IITI-3** for 24 hours resulted in morphological abnormalities of their cell shape. Untreated *Msm* demonstrated smooth, uniform, and slightly wrinkled cell structure (Fig. 3C-a). After treatment with **IITI-3** or **INH@IITI-3**, the bacterial cells displayed a loss in cellular integrity. The cells were irregular, longer and bulbous with a rough and wrinkled surface when exposed to **INH@IITI-3** as shown in (Fig. 3C-b). Likewise, **IITI-3** treated *Msm* displayed irregular, wrinkled, and destructed cell wall (Fig. 3C-c). We did not observe any change in the bacterial structure when treated with **INH** (Fig. 3C-d). These results suggest that **INH**-incorporated **IITI-3** has the potency to destruct the *Msm* cell wall, thereby effectively killing the bacteria.

3.4 Inhibition of biofilm formation by INH-encapsulated IITI-3

Biofilms are associated with several microbial infections leading to serious clinical complications.[9,94] The emergent properties of microbial biofilms, especially mycobacterial biofilms, include increased resistance to antibiotics and antimicrobial agents that may result in treatment failure.[95,96] Thus, a comparative anti-biofilm potential of newly synthesized **INH@IITI-3** and **INH** was performed against *Msm.* As the bound crystal violet was measured after 5 days of incubation, Fig. 4A shows a significant reduction in the biofilm formation in **INH@IITI-3** treated *Msm* as compared with **IITI-3** and buffer control treated *Msm*. There was a marked inhibition of biofilm formation in **INH**-treated *Msm.* However, the measurement of bound crystal violet for dispersed biofilm quantification showed no significant reduction in the biofilms after 5 days of treatment, indicating no substantial difference in the biofilm disruption Fig. 4B. From the above result, it can be suggested that **INH@IITI-3** has potential anti-biofilm activity against *Msm.*

Next, to corroborate the inhibition in biofilm formation, Acridine orange staining was performed. Microscopic analysis revealed significantly reduced, thin and scattered biofilms of **INH@IITI-3** (Fig. 4C-b) treated *Msm* as compared to the highly dense, compact, and well-structured biofilms of only *Msm* control (Fig. 4C-a) and **INH** (Fig. 4C-d) treated *Msm* (Fig. 4C). Moreover, lesser dense and slightly scattered biofilms were observed in **IITI-3**-treated *Msm* (Fig. 4C-c). From the above data, it can be suggested that **INH@IITI-3** has the potential to

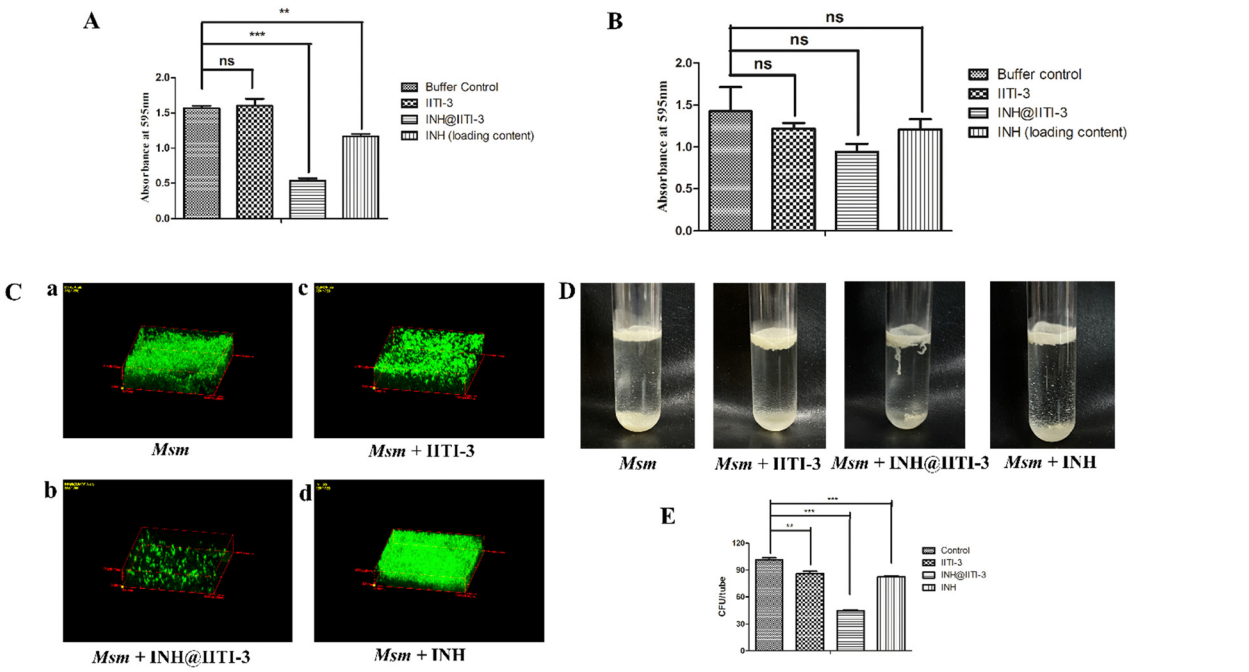

Fig. 4 Biofilm assay of *M. smegmatis* using **IITI-3**, **INH@IITI-3** and **INH** to determine (A) biofilm formation and (B) biofilm disruption, by crystal violet staining. (C) Acridine orange staining to determine the biofilm formation with various treatments using Confocal Laser Scanning Microscopy (CLSM). (D) Pellicle formation assay to determine the bacterial growth at the air–liquid interface with **IITI-3**, **INH@IITI-3** and **INH** treatment. (E) Determination of bacterial count post pellicle formation using the CFU assay.

 This journal is © The Royal Society of Chemistry 2023

Published on 24 2023. Downloaded on 29/07/25 17:07:55.

destruct the formed biofilms, thus indicating its possibility to exterminate biofilm infections during TB treatment.

Mycobacteria have the ability to form floating biofilms at the interface between air and liquid, known as the pellicle. Bacterial cells present within biofilm or pellicle are more resistant to antibiotic therapies and undergo horizontal transfer of antibiotic resistance genes among themselves.[97] Studies suggest that isolates and mutants of Gram-negative bacteria such as *Salmonella enterica* and *Pseudomonas aeruginosa* demonstrate a strong relationship between pellicle formation and biofilm forming ability.[98,99] A study by Chen *et al.*, 2006 reports *M. smegmatis lsr2* mutant was unable to form pellicles and was also defective in biofilm formation.[100] Similarly, overexpression of *rv1288* in *M. smegmatis* resulted in enhanced pellicle growth and aggregate formation indicating its link with the changed lipid composition of the cell wall.[101] Herein, we studied the effect of the synthesized compounds on the *Msm* pellicle. We observed thick, intact, and enhanced pellicles for control *Msm*, **IITI-3**-treated *Msm*, and **INH**-treated *Msm* (Fig. 4D). Additionally, the pellicle of **INH@IITI-3** treated *Msm* exhibited reduced capability to remain attached and was visualized to be loose and easily disturbed (Fig. 4D). Next, bacterial enumeration was performed by CFU assay, where we observed significantly reduced bacterial count in **INH@IITI-3** treated *Msm.* Bacterial enumeration of **IITI-3**/**INH** treated *Msm* also indicated reduced bacterial count as compared to control *Msm* pellicle (Fig. 4E). Together, these results demonstrate that **INH@IITI-3** is effective against *Msm* biofilms and pellicles, and with further studies, it can be effectively used in TB therapeutics.

3.5 Cytotoxicity study on mouse macrophages

Nanomaterials have a large surface area, making them better agents for various biological applications.[102] Thus, determining the toxicity of synthesized nanomaterials is very critical. Despite the extensive use of **INH** for TB treatment, there are several toxic side effects associated with **INH**.[103,104] Here, a comparative analysis of the cytotoxic action of **IITI-3**, **INH@IITI-3**, and **INH** has been performed against murine macrophages (RAW 246.7). After 24 hours of incubation with various concentrations of each molecule, cell viability has been determined. Fig. 5A indicates that cells treated with **IITI-3** and **INH** alone did not show any toxic effects; however, with the increase in the concentration (25 μg mL^{-1}) of **INH@IITI-3**, the viability of cells has decreased. The obtained data suggests that a higher concentration of **INH@IITI-3** leads to a slight decrease in the cell viability. To further validate the effect of the synthesized and drug incorporated MOFs on macrophage morphology, cells

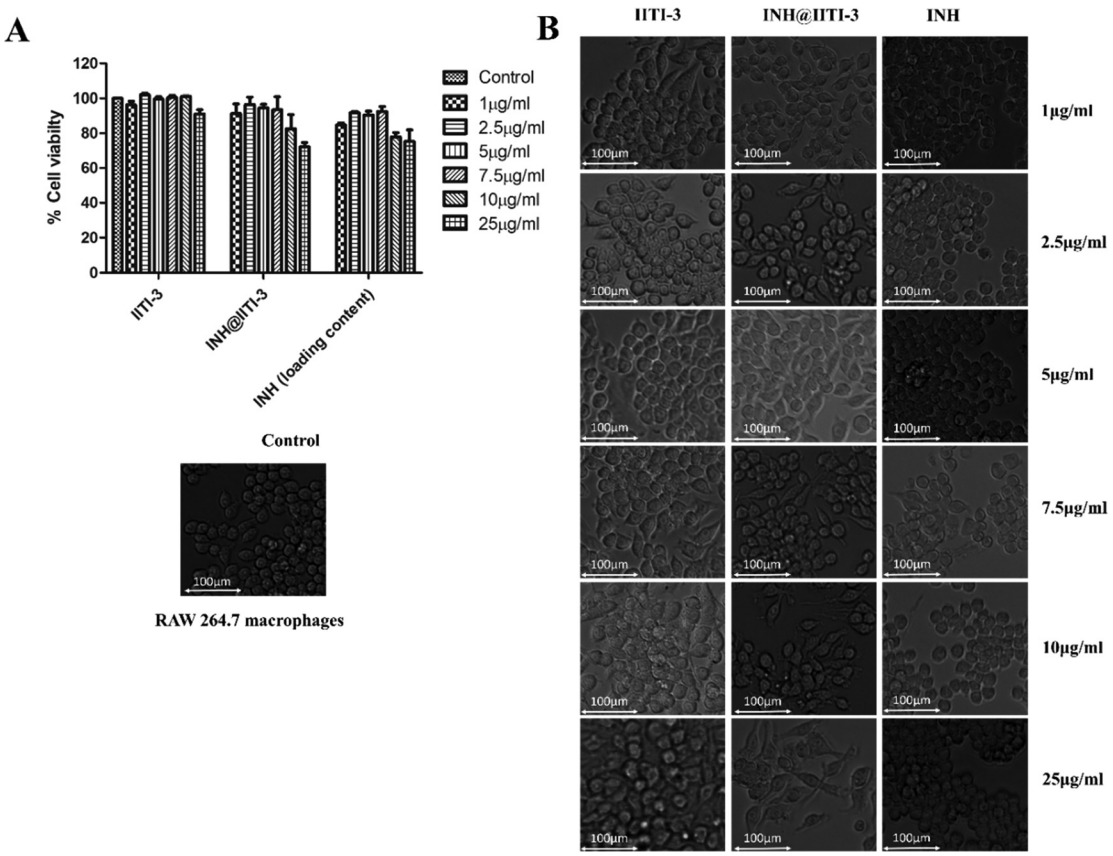

Fig. 5 *In vitro* cytotoxicity of **IITI-3**, **INH@IITI-3** and **INH** was determined in (A) RAW 264.7 murine macrophages. Cells were treated with different concentrations of compounds for 24 hours and CCK-8 analysis was performed to check the viability. (B) Bright-field microscopy images of macrophages after treatment with different concentrations of the compounds.

Published on 24 2023. Downloaded on 29/07/25 17:07:55.

were visualized under the light microscope. As shown in Fig. 5B, **IITI-3** and **INH** alone treated RAW 264.7 macrophages showed negligible cytotoxic effect with no damage to the cell morphology.

However, with an increase in the concentration of **INH@IITI-3**, macrophages exhibited few pseudopodia formation which could be due to the effect of the compound on the cells. These results imply that **INH@IITI-3** could be a promising candidate for therapeutic applications.

4. Conclusion

In this research work, **IITI-3** has been synthesized successfully. **IITI-3** has a large surface area and is mesoporous in nature. Furthermore, **IITI-3** was incorporated with **INH** to form **INH@IITI-3**. The prepared **INH@IITI-3** is well characterized by different physiochemical methods. The drug loading content is 10 wt% within 1 hour of time. Further drug release kinetics has been studied at two different pH values mimicking the small intestine and blood pH conditions, and the results showed that drug release behaviour follows first-order kinetics with an R^2 value of 0.9 which corresponds to drug release continuously with different rates. Furthermore, **INH@IITI-3** presented significant antimicrobial properties against *Msm* and BCG that were evident from the *in vitro* studies and morphological analysis. The study provides an overview of potential **INH@IITI-3** that holds promise in inhibiting mycobacterial biofilms and pellicles. A better understanding of **INH@IITI-3** and its underlying mechanism on the pathogenic TB strains could play an important role in developing more active, less toxic TB therapy approaches and in lowering the prevalence of *Mtb* treatment failures.

Conflicts of interest

There are no conflicts of interest to declare.

Acknowledgements

S. M. M. acknowledges BRNS (project no. 58/14/17/2020-BRNS/37215), and IIT Indore for financial support. P. K. would like to thank the Ministry of Education, Government of India, for providing a research fellowship. This work was supported by an Indo-Russian joint research grant (INT/RUS/RFBR/380) from the Department of Science and Technology, Government of India, to A. S. P. T. thanks BRNS (project no. 58/14/17/2020-BRNS/37215). The authors gratefully acknowledge Dr Ravinder, Mr Kinny Pandey, Mr Ghanashyam Bhavsar, and Dr Nitin Upadhyay (Sophisticated Instrumentation Centre, IIT Indore) for their help during characterization studies. The authors are also thankful to Material Research Centre, MNIT Jaipur, for proving the DLS and zeta potential facility. The authors are also thankful to Mr Ravindra Vishwakarma and Dr Tridib K. Sharma, Department of Chemistry IIT Indore, for providing DLS and Zetasizer facility. P. K. also thanks Dr Diptangshu Datta Mal, Dr Navpreet Kaur, and Praveen Kumar for their help with manuscript preparation. The authors would also like to thank the members of the A. S. lab and S. M. M. lab for fruitful suggestions and discussions.

References

1 Global tuberculosis report 2021, **https://www.who.int/publications-detail-redirect/9789240037021**, (accessed August 28, 2022).
2 G. Sotgiu, R. Centis, L. D'ambrosio and G. B. Migliori, *Cold Spring Harbor Perspect. Med.*, 2015, **5**, a017822.
3 R. E. Maphasa, M. Meyer and A. Dube, *Front. Cell. Infect. Microbiol.*, 2021, **10**, 618414.
4 Host-directed therapies for bacterial and viral infections|-Nature Reviews Drug Discovery, **https://www.nature.com/articles/nrd.2017.162**, (accessed April 24, 2023).
5 M. Badrinath and S. John, *StatPearls*, StatPearls Publishing, Treasure Island (FL), 2023.
6 A. Solokhina, D. Brückner, G. Bonkat and O. Braissant, *Sci. Rep.*, 2017, **7**, 9225.
7 L. K. Vestby, T. Grønseth, R. Simm and L. L. Nesse, *Antibiotics*, 2020, **9**, 59.
8 E. Roilides, M. Simitsopoulou, A. Katragkou and T. J. Walsh, *Microbiol. Spectrum*, 2015, **3**, 3.3.22.
9 J. P. Richards and A. K. Ojha, *Microbiol. Spectrum*, 2014, **2**, 2.5.16.
10 C. A. Fux, J. W. Costerton, P. S. Stewart and P. Stoodley, *Trends Microbiol.*, 2005, **13**, 34–40.
11 W. C. Reygaert, *AIMS Microbiol.*, 2018, **4**, 482–501.
12 O. Ciofu, E. Rojo-Molinero, M. D. Macià and A. Oliver, *APMIS*, 2017, **125**, 304–319.
13 H. Wu, C. Moser, H.-Z. Wang, N. Høiby and Z.-J. Song, *Int. J. Oral. Sci.*, 2015, **7**, 1–7.
14 S. Adepu and S. Ramakrishna, *Molecules*, 2021, **26**, 5905.
15 Z. Dong, Y. Sun, J. Chu, X. Zhang and H. Deng, *J. Am. Chem. Soc.*, 2017, **139**, 14209–14216.
16 R. Langer, *Acc. Chem. Res.*, 2000, **33**, 94–101.
17 J. Jacob, J. T. Haponiuk, S. Thomas and S. Gopi, *Mater. Today Chem.*, 2018, **9**, 43–55.
18 L. Pasqua, I. E. D. Napoli, M. D. Santo, M. Greco, E. Catizzone, D. Lombardo, G. Montera, A. Comandè, A. Nigro, C. Morelli and A. Leggio, *Nanoscale Adv.*, 2019, **1**, 3269–3278.
19 E. Bagheri, L. Ansari, K. Abnous, S. M. Taghdisi, F. Charbgoo, M. Ramezani and M. Alibolandi, *J. Controlled Release*, 2018, **277**, 57–76.
20 J.-J. Zou, G. Wei, C. Xiong, Y. Yu, S. Li, L. Hu, S. Ma and J. Tian, *Sci. Adv.*, 2022, **8**, eabm4677.
21 S. Furukawa, J. Reboul, S. Diring, K. Sumida and S. Kitagawa, *Chem. Soc. Rev.*, 2014, **43**, 5700–5734.
22 H. Li, M. Eddaoudi, M. O'Keeffe and O. M. Yaghi, *Nature*, 1999, **402**, 276–279.
23 H. C. Zhou, J. R. Long and O. M. Yaghi, *Chem. Rev.*, 2012, **112**, 673–674.

 This journal is © The Royal Society of Chemistry 2023

Published on 24 2023. Downloaded on 29/07/25 17:07:55.

24 Y. Chen, P. Li, J. A. Modica, R. J. Drout and O. K. Farha, *J. Am. Chem. Soc.*, 2018, **140**, 5678–5681.
25 O. M. Yaghi, G. Li and H. Li, *Nature*, 1995, **378**, 703–706.
26 L. Robison, X. Gong, A. M. Evans, F. A. Son, X. Wang, L. R. Redfern, M. C. Wasson, Z. H. Syed, Z. Chen, K. B. Idrees, T. Islamoglu, M. Delferro, W. R. Dichtel, F.-X. Coudert, N. C. Gianneschi and O. K. Farha, *J. Am. Chem. Soc.*, 2021, **143**, 1503–1512.
27 Z. Chen, M. R. Mian, S.-J. Lee, H. Chen, X. Zhang, K. O. Kirlikovali, S. Shulda, P. Melix, A. S. Rosen, P. A. Parilla, T. Gennett, R. Q. Snurr, T. Islamoglu, T. Yildirim and O. K. Farha, *J. Am. Chem. Soc.*, 2021, **143**, 18838–18843.
28 J. Tian, Z.-Y. Xu, D.-W. Zhang, H. Wang, S.-H. Xie, D.-W. Xu, Y.-H. Ren, H. Wang, Y. Liu and Z.-T. Li, *Nat. Commun.*, 2016, **7**, 11580.
29 L. Zhang, Z. Liu, Q. Deng, Y. Sang, K. Dong, J. Ren and X. Qu, *Angew. Chem., Int. Ed.*, 2021, **60**, 3469–3474.
30 Q. Xia, W. Li, X. Zou, S. Zheng, Z. Liu, L. Li and F. Yan, *Mater. Horiz.*, 2022, **9**, 2881–2892.
31 M. Mirzaei, H. Eshtiagh-Hosseini, Z. Karrabi, K. Molčanov, E. Eydizadeh, J. T. Mague, A. Bauzá and A. Frontera, *CrystEngComm*, 2014, **16**, 5352–5363.
32 M. Bazargan, M. Mirzaei, A. Franconetti and A. Frontera, *Dalton Trans.*, 2019, **48**, 5476–5490.
33 Z. Rahmati, R. Khajavian and M. Mirzaei, *Inorg. Chem. Front.*, 2021, **8**, 3581–3586.
34 M. Bazargan, M. Mirzaei, A. Amiri and C. Ritchie, *Microchim. Acta*, 2021, **188**, 108.
35 O. K. Farha, I. Eryazici, N. C. Jeong, B. G. Hauser, C. E. Wilmer, A. A. Sarjeant, R. Q. Snurr, S. T. Nguyen, A. Ö. Yazaydın and J. T. Hupp, *J. Am. Chem. Soc.*, 2012, **134**, 15016–15021.
36 G. Li and Y. Han, *ACS Cent. Sci.*, 2022, **8**, 150–152.
37 N. Singh, S. Qutub and N. M. Khashab, *J. Mater. Chem. B*, 2021, **9**, 5925–5934.
38 Z. Chao, J. Li, W. Jiang, C. Zhang, J. Ji, X. Hua, L. Xu, L. Han and L. Jia, *Mater. Chem. Front.*, 2021, **5**, 7617–7627.
39 W. Zhu, J. Guo, J. O. Agola, J. G. Croissant, Z. Wang, J. Shang, E. Coker, B. Motevalli, A. Zimpel, S. Wuttke and C. J. Brinker, *J. Am. Chem. Soc.*, 2019, **141**, 7789–7796.
40 K. Wang, Y. Li, L.-H. Xie, X. Li and J.-R. Li, *Chem. Soc. Rev.*, 2022, **51**, 6417–6441.
41 A. Hassanpoor, M. Mirzaei, M. N. Shahrak and A. M. Majcher, *Dalton Trans.*, 2018, **47**, 13849–13860.
42 A. Abdar, A. Amiri and M. Mirzaei, *J. Chromatogr. A*, 2023, **1707**, 464295.
43 A. Abdar, A. Amiri and M. Mirzaei, *Microchem. J.*, 2022, **177**, 107269.
44 S. Ghanei-Zare, M. Moghadasi, R. Khajavian, N. Akbarzadeh-T and M. Mirzaei, *J. Mol. Struct.*, 2023, **1286**, 135563.
45 R. Khajavian, M. Mirzaei and H. Alizadeh, *Dalton Trans.*, 2020, **49**, 13936–13947.
46 M. Bazargan, F. Ghaemi, A. Amiri and M. Mirzaei, *Coord. Chem. Rev.*, 2021, **445**, 214107.
47 A. Amiri and M. Mirzaei, RSC 2023 ebook collection, DOI: **10.1039/9781839167485**.
48 J. Yang and Y.-W. Yang, *Small*, 2020, **16**, 1906846.
49 H. Sohrabi, S. Ghasemzadeh, S. Shakib, M. R. Majidi, A. Razmjou, Y. Yoon and A. Khataee, *Ind. Eng. Chem. Res.*, 2023, **62**, 4611–4627.
50 K. S. Butler, C. J. Pearce, E. A. Nail, G. A. Vincent and D. F. Sava Gallis, *ACS Appl. Mater. Interfaces*, 2020, **12**, 31217–31224.
51 A. López-Olvera, J. G. Flores, J. Aguilar-Pliego, C. K. Brozek, A. Gutiérrez-Alejandre and I. A. Ibarra, *Chem. Mater.*, 2021, **33**, 6269–6276.
52 Y. Yu, G. Chen, J. Guo, Y. Liu, J. Ren, T. Kong and Y. Zhao, *Mater. Horiz.*, 2018, **5**, 1137–1142.
53 M. Nazari, A. S. Saljooghi, M. Ramezani, M. Alibolandi and M. Mirzaei, *J. Mater. Chem. B*, 2022, **10**, 8824–8851.
54 Z. Zhang, H. Zhang, D. Tian, A. Phan, M. Seididamyeh, M. Alanazi, Z. Ping Xu, Y. Sultanbawa and R. Zhang, *Coord. Chem. Rev.*, 2024, **498**, 215455.
55 Z. Sun, T. Li, T. Mei, Y. Liu, K. Wu, W. Le and Y. Hu, *J. Mater. Chem. B*, 2023, **11**, 3273–3294.
56 M. Moharramnejad, A. Ehsani, M. Shahi, S. Gharanli, H. Saremi, R. E. Malekshah, Z. S. Basmenj, S. Salmani and M. Mohammadi, *J. Drug Delivery Sci. Technol.*, 2023, **81**, 104285.
57 M. A. Simon, E. Anggraeni, F. E. Soetaredjo, S. P. Santoso, W. Irawaty, T. C. Thanh, S. B. Hartono, M. Yuliana and S. Ismadji, *Sci. Rep.*, 2019, **9**, 16907.
58 G. Wyszogrodzka-Gaweł, P. Dorożyński, S. Giovagnoli, W. Strzempek, E. Pesta, W. P. Węglarz, B. Gil, E. Menaszek and P. Kulinowski, *Pharmaceutics*, 2019, **11**, 687.
59 A. P. Acharya, K. B. Sezginel, H. P. Gideon, A. C. Greene, H. D. Lawson, S. Inamdar, Y. Tang, A. J. Fraser, K. V. Patel, C. Liu, N. L. Rosi, S. Y. Chan, J. L. Flynn, C. E. Wilmer and S. R. Little, *J. Controlled Release*, 2022, **352**, 242–255.
60 K. Sun, L. Li, X. Yu, L. Liu, Q. Meng, F. Wang and R. Zhang, *J. Colloid Interface Sci.*, 2017, **486**, 128–135.
61 C. Gajadeera, M. J. Willby, K. D. Green, P. Shaul, M. Fridman, S. Garneau-Tsodikova, J. E. Posey and O. V. Tsodikov, *J. Antibiot.*, 2015, **68**, 153–157.
62 P. Kumar, N. Kaur, P. Tiwari, A. K. Gupta and S. M. Mobin, *ACS Mater. Lett.*, 2023, **5**, 1100–1108.
63 X. Zhang, Z. Chen, X. Liu, S. L. Hanna, X. Wang, R. Taheri-Ledari, A. Maleki, P. Li and O. K. Farha, *Chem. Soc. Rev.*, 2020, **49**, 7406–7427.
64 A. J. Howarth, A. W. Peters, N. A. Vermeulen, T. C. Wang, J. T. Hupp and O. K. Farha, *Chem. Mater.*, 2017, **29**, 26–39.
65 J. E. Mondloch, O. Karagiaridi, O. K. Farha and J. T. Hupp, *CrystEngComm*, 2013, **15**, 9258–9264.
66 Y. Zhou, L. Liu, Y. Cao, S. Yu, C. He and X. Chen, *ACS Appl. Mater. Interfaces*, 2020, **12**, 22581–22592.
67 R. Pati, R. Sahu, J. Panda and A. Sonawane, *Sci. Rep.*, 2016, **6**, 24184.
68 A. Padhi, S. K. Naik, S. Sengupta, G. Ganguli and A. Sonawane, *Microbes Infect.*, 2016, **18**, 224–236.
69 S. N. Ansari, P. Kumar, A. K. Gupta, P. Mathur and S. M. Mobin, *Inorg. Chem.*, 2019, **58**, 9723–9732.
70 A. Kawamura, A. R. Greenwood, A. S. Filatov, A. T. Gallagher, G. Galli and J. S. Anderson, *Inorg. Chem.*, 2017, **56**, 3349–3356.

Published on 24 2023. Downloaded on 29/07/25 17:07:55.

71 Y. Zeng, T. Lan, M. Li, G. Yuan, F. Li, J. Liao, J. Yang, Y. Yang and N. Liu, *J. Chem. Eng. Data*, 2021, **66**, 749–760.
72 D. Liu, Y.-J. Chang and J.-P. Lang, *CrystEngComm*, 2011, **13**, 1851–1857.
73 H. V. Doan, H. Amer Hamzah, P. Karikkethu Prabhakaran, C. Petrillo and V. P. Ting, *Nano-Micro Lett.*, 2019, **11**, 54.
74 L. Peng, S. Yang, S. Jawahery, S. M. Moosavi, A. J. Huckaba, M. Asgari, E. Oveisi, M. K. Nazeeruddin, B. Smit and W. L. Queen, *J. Am. Chem. Soc.*, 2019, **141**, 12397–12405.
75 P. Horcajada, T. Chalati, C. Serre, B. Gillet, C. Sebrie, T. Baati, J. F. Eubank, D. Heurtaux, P. Clayette, C. Kreuz, J.-S. Chang, Y. K. Hwang, V. Marsaud, P.-N. Bories, L. Cynober, S. Gil, G. Férey, P. Couvreur and R. Gref, *Nat. Mater.*, 2010, **9**, 172–178.
76 G. Férey, *Chem. Soc. Rev.*, 2007, **37**, 191–214.
77 S. Rojas, I. Colinet, D. Cunha, T. Hidalgo, F. Salles, C. Serre, N. Guillou and P. Horcajada, *ACS Omega*, 2018, **3**, 2994–3003.
78 J. A. Kellum, *Crit. Care*, 2000, **4**, 6.
79 Z. Li, Y. Peng, X. Xia, Z. Cao, Y. Deng and B. Tang, *Sci. Rep.*, 2019, **9**, 17570.
80 B. E. Souza, L. Donà, K. Titov, P. Bruzzese, Z. Zeng, Y. Zhang, A. S. Babal, A. F. Möslein, M. D. Frogley, M. Wolna, G. Cinque, B. Civalleri and J.-C. Tan, *ACS Appl. Mater. Interfaces*, 2020, **12**, 5147–5156.
81 M. Chakraborty, S. Dasgupta, C. Soundrapandian, J. Chakraborty, S. Ghosh, M. K. Mitra and D. Basu, *J. Solid State Chem.*, 2011, **184**, 2439–2445.
82 C. X. (Cynthia) Lin, S. Z. Qiao, C. Z. Yu, S. Ismadji and G. Q. (Max) Lu, *Microporous Mesoporous Mater.*, 2009, **117**, 213–219.
83 P. Costa and J. M. S. Lobo, *Eur. J. Pharm. Sci.*, 2001, **13**(2), 123–133.
84 *Strategies to Modify the Drug Release from Pharmaceutical Systems*, ed. M. L. Bruschi, Woodhead Publishing, 2015, pp. 63–86.
85 R. Yoshida, K. Sakai, T. Okano and Y. Sakurai, *Polym. J.*, 1991, **23**, 1111–1121.
86 N. V. Mulye and S. J. Turco, *Drug Dev. Ind. Pharm.*, 1995, **21**, 943–953.
87 J. V. Natarajan, C. Nugraha, X. W. Ng and S. Venkatraman, *J. Controlled Release*, 2014, **193**, 122–138.
88 D. D. Mal, S. Khilari and D. Pradhan, *Green Chem.*, 2018, **20**, 2279–2289.
89 K. Jiang, L. Zhang, Q. Hu, X. Zhang, J. Zhang, Y. Cui, Y. Yang, B. Li and G. Qian, *Microporous Mesoporous Mater.*, 2019, **275**, 229–234.
90 H. Wu, Q. Geng, Y. Li, Y. Song, J. Chu, R. Zhou, X. Ning, S. Dong and D. Yuan, *J. Ind. Eng. Chem.*, 2022, **114**, 475–482.
91 D. Han, X. Liu and S. Wu, *Chem. Soc. Rev.*, 2022, **51**, 7138–7169.
92 M. Yang, J. Zhang, Y. Wei, J. Zhang and C. Tao, *Nano Res.*, 2022, **15**, 6220–6242.
93 J. H. Jo, H.-C. Kim, S. Huh, Y. Kim and D. N. Lee, *Dalton Trans.*, 2019, **48**, 8084–8093.
94 Frontiers|Beyond Risk: Bacterial Biofilms and Their Regulating Approaches, **https://www.frontiersin.org/articles/10.3389/fmicb.2020.00928/full**, (accessed April 24, 2023).
95 J. Esteban and M. García-Coca, *Front. Microbiol.*, 2018, **8**, 2651.
96 H.-C. Flemming, J. Wingender, U. Szewzyk, P. Steinberg, S. A. Rice and S. Kjelleberg, *Nat. Rev. Microbiol.*, 2016, **14**, 563–575.
97 C. Michaelis and E. Grohmann, *Antibiotics*, 2023, **12**, 328.
98 L. Friedman and R. Kolter, *Mol. Microbiol.*, 2003, **51**, 675–690.
99 C. Solano, B. García, J. Valle, C. Berasain, J.-M. Ghigo, C. Gamazo and I. Lasa, *Mol. Microbiol.*, 2002, **43**, 793–808.
100 J. M. Chen, G. J. German, D. C. Alexander, H. Ren, T. Tan and J. Liu, *J. Bacteriol.*, 2006, **188**, 633–641.
101 P. Maan, A. Kumar, J. Kaur and J. Kaur, *Front. Cell. Infect. Microbiol.*, 2018, **8**, 421.
102 O. Salata, *J. Nanobiotechnol.*, 2004, **2**, 3.
103 E. R. Erwin, A. P. Addison, S. F. John, O. A. Olaleye and R. C. Rosell, *Tuberculosis*, 2019, **116**, S66–S70.
104 M. Combrink, D. T. Loots and I. du Preez, *Toxicol. Lett.*, 2020, **322**, 104–110.

This journal is © The Royal Society of Chemistry 2023